Nanoscale

PAPER

View Article Online
View Journal

Cite this: DOI: 10.1039/d2nr06783h

Degradation of methyl orange by dielectric films based on contact-electro-catalysis†

Xin Zhao,‡[a] Yusen Su, ‡[a,b] Andy Berbille,[a,b] Zhong Lin Wang *[a,b,c] and Wei Tang *[a,b]

Contact-electro-catalysis (CEC) has been recently proposed for the effective degradation of methyl orange, but the reactivity of catalysts in the CEC process needs further investigation. Here, we have used dielectric films, such as fluorinated ethylene propylene (FEP), modified by inductively coupled plasma (ICP) etching with argon, to replace the previously employed micro-powder due to their potential scalability, facile recycling process, and possible lower generation of secondary pollution. It has been found that ICP creates cone-like micro/nano structures on the surface, and thus changes the contact angle and specific surface area. The value of the contact angle varies non-linearly with etching time and attains a maximum after 60 seconds of etching. Concurrently, an increased electron transfer is observed, as well as an enhanced degradation efficiency, thus suggesting a special role of the surface structure. Finally, KPFM measurements show a lower electron affinity at the summit of the nanocones. This observation suggests that the structures are endowed with higher charge transfer ability. In addition, this film-based CEC has been observed in several polymer materials, such as PET, PTFE, and PVC. We view this work as a stepping stone to develop CEC into scalable applications, based on film technologies.

Received 4th December 2022,
Accepted 23rd February 2023

DOI: 10.1039/d2nr06783h

rsc.li/nanoscale

Introduction

The presence of dyes in water has become a serious problem for biological organisms.[1] Since dyes are widely used in textiles, cosmetics, plastics, food, papermaking, *etc*, more than 10 000 000 tons of dyes are produced worldwide each year.[2] Most of them, which are azo dyes,[3] cannot be treated by conventional wastewater treatment processes owing to their stable structures. The Fenton reaction gifted us with a cheap source of free hydroxyl radicals by using H_2O_2 and Fe^{2+} ions.[4,5] Although these methods allow the destruction of refractory organic compounds, the introduction of heavy metal ions as secondary pollutants is a significant limitation.[6]

Despite the significant progress made in wastewater treatment,[7–10] research for the development of more eco-friendly processes is needed. In the last few decades, scientists introduced several Fenton-like processes,[11–13] which rely on electrochemical principles and nanotechnologies to address the issues aforementioned.[14] Various strategies have been adopted to degrade azo dyes, such as electrocatalysis,[15,16] photocatalysis,[17,18] piezocatalysis,[19–21] and biochemical methods.[22–24] However, these methods suffer from several drawbacks. For example, electrocatalysis can be hindered by poor mass transfer in the absence of proper agitation,[25] and in photocatalysis the efficiency is the highest at the surface of the solution.[26] Input of mechanical energy could alleviate these issues, and piezocatalysis is a good candidate for this, but similarly to the two aforementioned technics it requires the use of metals and semiconducting materials to perform.[20] Finally, biochemical methods, despite their many advantages, suffer from lower degradation rates.[27]

More recently, contact-electrification-catalysis (CEC) for the degradation of azo dyes in contaminated water was first introduced.[28] CEC is based on the principles of liquid–solid contact electrification, which has been observed at the liquid–insulator,[29] liquid–semiconductor,[30,31] and liquid–metal[32] interface. Pristine polymers, such as polytetrafluoroethylene[33] (PTFE) and fluorinated ethylene propylene[34] (FEP), possess the ability to withdraw electrons from deionized water during the process of contact electrification. Furthermore, it has been suggested that electron transfers could dominate the transfer process during water-dielectric contact-electrification in some instances.[35] The electron-cloud-potential-well model has been proposed to explain the mechanism of electron transfers during contact-electrification.[36,37] Following the path drawn by

[a]CAS Center for Excellence in Nanoscience, Beijing Institute of Nanoenergy and Nanosystems, Chinese Academy of Sciences, Beijing, 100083, China. E-mail: tangwei@binn.cas.cn, zhong.wang@mse.gatech.edu
[b]School of Nanoscience and Technology, University of Chinese Academy of Sciences, Beijing, 100049, China
[c]Georgia Institute of Technology, Atlanta, GA 30332-0245, USA

†Electronic supplementary information (ESI) available. See DOI: https://doi.org/10.1039/d2nr06783h

‡These authors contributed equally to this work.

former experimental and theoretical research, contact-electro-catalysis has been proposed as another application of liquid–solid contact-electrification.[38] CEC utilizes ultrasound to trigger exchange of electrons between water and dielectric materials by contact electrification. To put it briefly, high-frequency ultrasound creates cavitation bubbles, which cause frequent contact electrification between fluorinated ethylene propylene (FEP) powder and water. Thus, electron transfer from water to the FEP surface occurs. These events subsequently result in the formation of reactive oxygen species, which are powerful oxidants. Previous work showed that various azo dyes such as methyl orange (MO) and acid orange 17 can be successfully degraded by employing this method.[28,38]

However, recycling of these dielectric powders requires filtration processes to avoid potential secondary pollution. Since we have proposed CEC-induced methyl orange degradation by FEP powder previously, we wondered if the same principle could apply to a film. In this work, we present a CEC process based on polymer films instead of powders. Additionally, surface modification by ICP etching has also been introduced, and its effect on the catalytic efficiency has been studied. Several chemical and physical characterization studies were conducted to find the relationship between surface modifications and degradation. Finally, we studied the effect of surface modifications on several different films, namely PET, PTFE, and PVC. Developing a film-based CEC process opens a path towards a scalable process unburdened by the need for filtration systems required in powder-based processes.

Results and discussion

Contact-electro-catalysis supported on films

Fig. 1 shows the results of contact-electro-catalysis (CEC) degradation based on films as well as the film modification process and a schematic diagram of the experimental method. The setup and processes of our experiment are illustrated in Fig. 1a. 50 μm thick FEP films were first coated with gold through a mask. Then, both sides were etched by the inductively coupled plasma (ICP) etching process. Afterwards, the as-prepared film was added to a 50 ml aqueous methyl orange (MO) solution (5 ppm), and the solution was ultrasonicated at a frequency of 40 kHz. Ultrasound was applied here to generate cavitation bubbles (CB) that cause contact and separation between the FEP film and the MO solution.[39] Fig. 1b shows the degradation results by FEP films. 2 mL of solution were sampled at pre-defined time intervals for analysis. UV-Vis spectroscopy was employed to measure the characteristic absorbance peaks of MO, at ~470 nm. It can be seen from Fig. 1b that the surface treatment by ICP significantly enhances the degradation rate and efficiency. Specifically, the pristine FEP film achieved 50% degradation after 5 hours, whereas that treated by ICP achieved 90% degradation in the same time period. As a comparison, experiments attempting the degradation of MO solution with/without high density polyethylene (HDPE, which is reported to possess lower contact-electrification properties[40,41]) films were conducted. 8% degradation and 10% degradation of MO were achieved after 5 hours of ultrasonication (Fig. S1†), which indicates that to obtain an

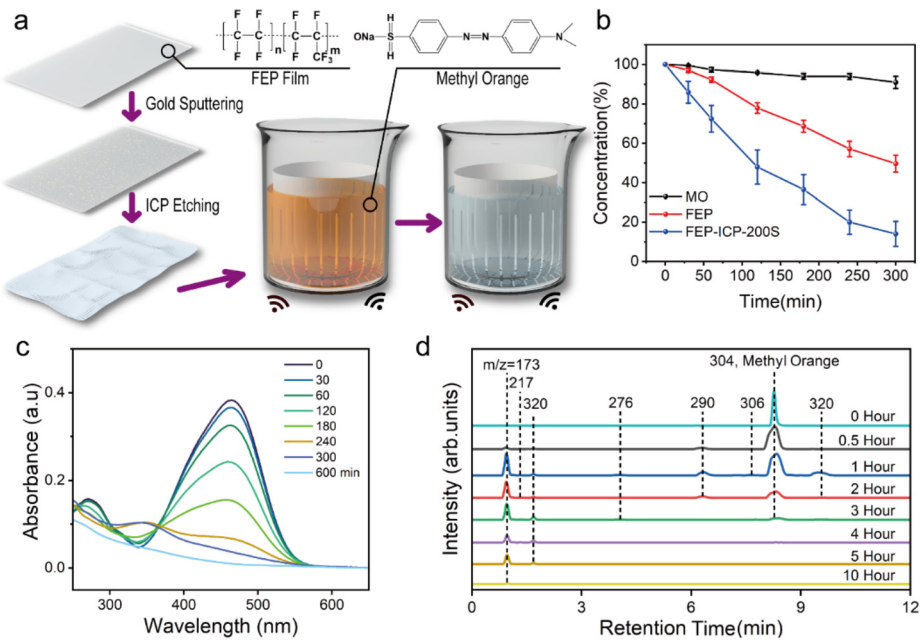

Fig. 1 Degradation of methyl orange by CEC supported on a film. (a) 3D schematic diagram of the experimental setup and process. (b) Absorbance of an MO solution during ultrasonication without any catalyst, with an FEP film and with an ICP-treated FEP film. (c) UV-Vis spectra of a MO solution during ultrasonication with the FEP film (etched for 200 seconds) for 10 hours. (d) Mass spectra of the MO solution after separation by liquid chromatography. Error bars represent the standard deviation based on three replicate data.

important CEC activity one has to select a dielectric film with suitable electrification properties. The degradation efficiency of films with poor CE properties can also be enhanced by surface modification, as shown in Fig. S2.† Fig. 1c shows that the MO peak decreased as the ultrasonication time increased, and approached zero after 600 min in the presence of the modified FEP film. Meanwhile, only a slight decrease in MO concentration was detected in the control group (ultrasonication without films) as shown in Fig. S3.† Note that the new peak at around 350 nm which appeared in 240 min and disappeared in 600 min is attributed to the byproducts of MO degradation. Liquid-chromatography mass-spectroscopy (LC-MS) was employed to detect the intermediate products of degradation. Chromatograms at different ultrasonication times in the presence of an etched FEP film are shown in Fig. 1d. All the peaks are labelled with the corresponding mass-to-charge ratios (m/z). The characteristic peak of MO, m/z of 304, appears at a retention time of 8.6 min. Its intensity decreased along with the formation of other peaks and disappeared after 4 hours of reaction. The degradation products of MO were identified (Fig. S4†) and they matched the results previously reported.[28]Almost all peaks disappeared after 10 hours of ultrasonication. Notably, the FEP film appears to be chemically inert in most of the chemical reactions and is widely used as a coating material. Here we have successfully utilized it as a catalyst for degrading an organic pollutant based on the CEC process.

Physical characterization of the modified FEP film

Scanning electron microscopy (SEM) images of FEP films etched at different times are presented in Fig. 2a. Argon gas was employed to avoid the adjunction of new groups at the surface. X-ray photoelectron spectroscopy (XPS) analyses of the FEP film before and after degradation were conducted to detect the vibration of chemical states at the surface of the FEP film. The F 1s, O 1s, and C 1s peaks of the FEP film are shown in Fig. S5.† The XPS spectra before and after the reaction do not present any clear changes, both in terms of peak shifting or number of peaks, suggesting that the chemical state of the FEP film did not change after argon gas etching. The gold mask originally applied was removed in the first 5 seconds of ICP etching.[42] Ridges and holes were observed in the SEM image after 20 seconds of etching. After 40 seconds of the same treatment, a nanoforest was generated. The formation of this nanoforest makes the surface very similar to that of a lotus leaf, making the FEP films nearly superhydrophobic. To study the influence of etching time of the FEP surface on its hydrophobic properties, static contact angle measurements were conducted on the films etched for various durations using the sessile drop method as shown in Fig. 2b. The blue dotted line shows that the original FEP film is characterized by an 80.398° contact angle before the ICP etching. After only 20 seconds of etching a slight increase in hydrophobicity is observed. The maximum contact angle of ~147.27° was observed after 60 seconds of etching, suggesting that the hydrophobicity of the FEP film does not increase monotonically with etching time. Indeed, beyond 60 seconds of treatment, the contact angle decreases slightly and stabilizes at around 120°. We believe that this tendency can be attributed to the formation of a steady-state layer on the surface after long-time etching.[43] The average area of a single rod was calculated from SEM images using ImageJ as shown in Fig. 2c. The size of a single nanocone reaches a maximum at 60 seconds. A maximum of ~158 nm diameter, 100 nm height, and

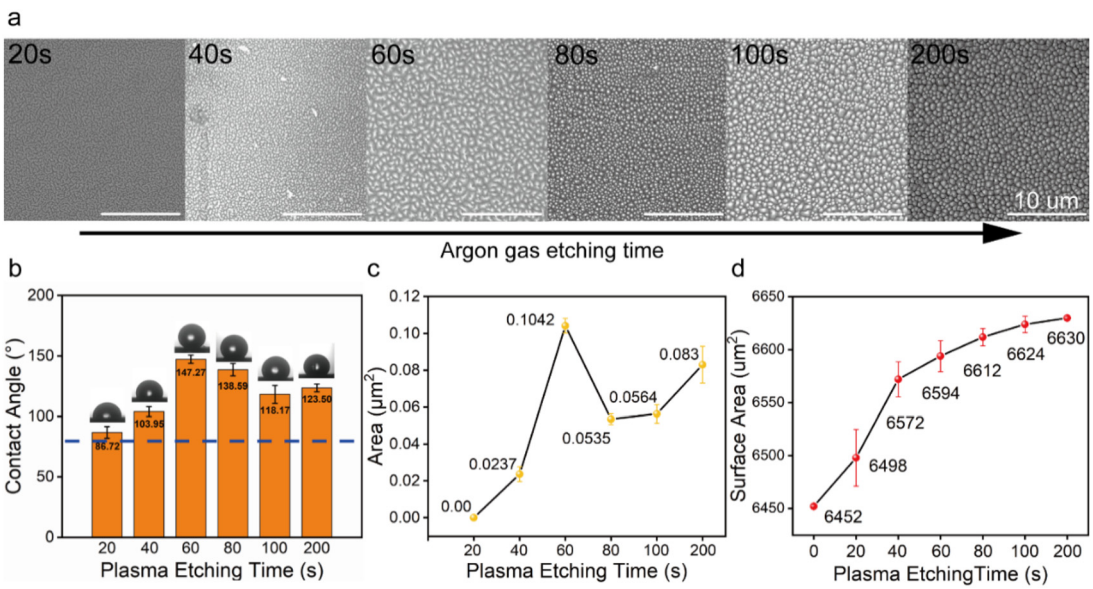

Fig. 2 Characterization of the modified FEP film surface structure. (a) SEM images of FEP films etched for different durations. (b) The contact angle of the FEP film with different etching times. The blue dashed line is the contact angle of the non-etched film. (c) The average surface occupied by the base of a single nanocone on the FEP film surface. (d) Surface area of the FEP film at different etching times. Error bars represent the standard deviation based on three replicate data.

~0.1042 μm^2 average surface occupied by the base of the nanocones are created by ICP processing. The 20-second modified film does not exhibit nanoforest structures. A correlation between the maximum nanocone area, the contact angle and SEM observations has been found. The film surface area for each etching time was measured by atomic fore microscopy (AFM), as shown in Fig. 2d. An 80 × 80 μm^2 area was scanned in three different films for each sample. The result shows that the surface area increased from ~6452 μm^2 to ~6594 μm^2 during the first 60 seconds of etching, and then slowly reached up to ~6630 μm^2. The lower influence of ICP etching on these parameters after 60 seconds could also be attributed to the formation of a steady-state layer with smaller surface structures. The surface area evolves non-linearly with etching time, following a power function behavior, which is different from the aforementioned trend observed for the surface, while surface roughness (see Fig. S6†) follows the previously described trend. This difference suggests that the surface area and surface structure play different roles when it comes to the physicochemical interaction at the interface of water and FEP. In the next part, we have studied the influence of plasma etching on charge exchanges and CEC degradation performance.

CEC and charge transfer of the modified FEP film

CEC is based on liquid–solid electron transfer. To investigate how the etching process influences charge transfer, a single electrode triboelectric nanogenerator (TENG) was employed to measure the performance of contact electrification at the water–FEP film interface. The structure and setup of the TENG experiment can be seen in Fig. S8.† The transferred charges in Fig. 3a between water and the FEP film increased from 9.3 nC to reach a maximum at 45.2 nC and then decreased to 31.2 nC, before it increased to 35.2 nC. The values of charges for one contact–separation cycle increased as cycles increased and reached a maximum, suggesting that charges are accumulated on the FEP film during contact with DI water. The results obtained follow a similar trend to that of the contact angle and the average cone surface area observed by SEM, suggesting the direct relationship between the surface structure and charge transfer ability. The contact-electro-catalysis (CEC) theory as shown in Fig. 3b has been proposed in former research.[28] The collapse of cavitation bubbles provides not only frequent contact–separation to provoke contact-electrification but also high pressure to increase the chance of electron cloud leap between the groups at the surface of FEP and water molecules. With high pressure and frequent contact-electrification, an electron is transferred from a H_2O molecule to the FEP film to form a water radical cation that rapidly decays to $^{\bullet}OH$. At the same time, oxygen accepts an electron from FEP to generate $^{\bullet}O_2^-$. $^{\bullet}OOH$ can be formed from $^{\bullet}O_2^-$ reacting with H_3O^+, later leading to the production of $^{\bullet}OH$.[28] This process will repeat as long as the ultrasonication continues.

To verify that CEC is responsible for the observation, we conducted experiments at various pH values as well as concentrations of NaCl solution. Indeed, if contact electrification is responsible for the observed chemical activity, we should observe a decrease in the generation of radicals as either ionic concentration or pH increases. The highest efficiency should be obtained in a neutral solution and at the lowest ion concentration. The results are shown in Fig. S9 and Fig. S10.† As expected, the lowest efficiency was observed at pH 11 and 3, or

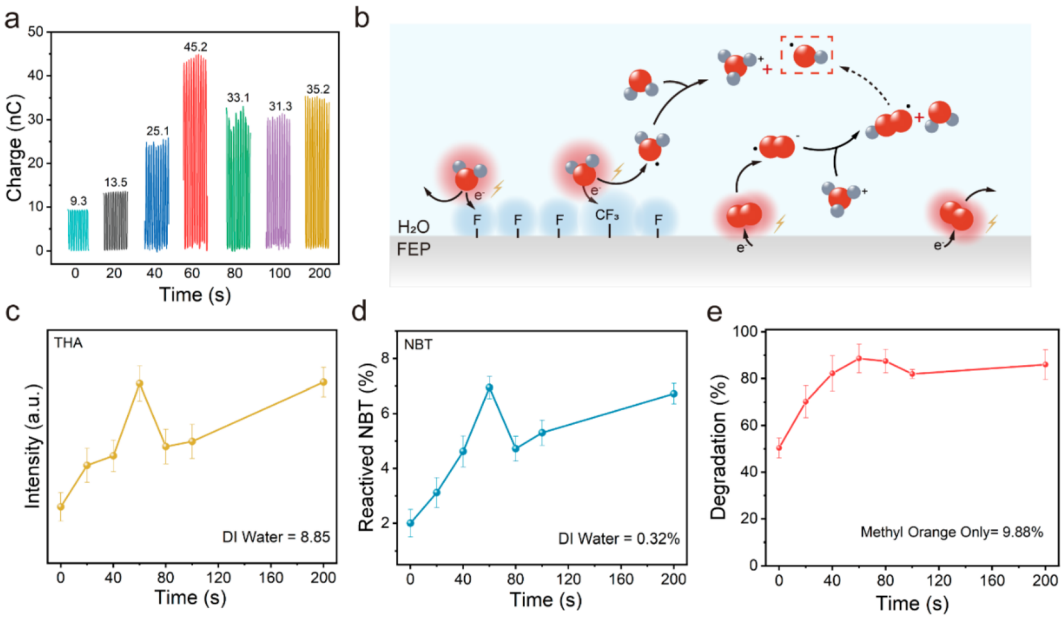

Fig. 3 CEC performance of the etched FEP film. (a) The measured charge output of a single electrode triboelectric nanogenerator (TENG) plunging repeatedly back and forth in DI water. The left inset shows the details of the output of the FEP film etched for 20 seconds. (b) Contact-electro-catalysis mechanism. Red balls and grey balls represent oxygen and hydrogen atoms, respectively. (c) Fluorescence intensity of THA-OH, (d) absorbance of formazan NBT, (e) degradation of MO at 20, 40, 60, 80, 100, and 200 seconds in the ICP etched FEP film.

as the NaCl concentration increased from 0 to 1 M. This observation was made for FEP, PTFE, PVC, and PET. Both changing the pH and introducing NaCl increased the concentration of ions in the solution. This induced a charge-screening effect that hindered electron transfer.[44] To further investigate the influence of the surface structure on the generation of free radicals, THA and NBT were employed to capture $OH^{\bullet}$ and $^{\bullet}O_2^-$ free radicals, respectively. The results shown in Fig. 3c and d follow a similar trend to that observed for degradation, transferred charges, and area of nano-cones. The results confirmed that film-based CEC can be employed to produce reactive oxygen species, and that nanostructures are able to improve the activity of the contact-electro-catalyst.

We also examined how the etching process influences charge transfer. The 5 hour degradation of MO by FEP films with various etching times is shown in Fig. 3e. The detailed degradation as a function of time of each kind of film is presented in Fig. S7.† Compared to a non-modified FEP film, ICP etching significantly increases the efficiency of pollutant degradation. The efficiency increases from 50% to a maximum of 90% with a 60 second etched-film and then slightly decreases to 80%, but finally increases to 88%. The trend of MO degradation is consistent with what has been observed for contact angle, SEM, and surface roughness results, but different from the surface area measurement in AFM. It can be seen that in the first 60 seconds of etching, the degradation curve is consistent with the change in the surface structure, both of which increase fast and reach the maximum at 60 seconds. Then, however, the CEC reaction efficiency did not decrease so much like the contact angle but the resulting SEM curve still showed another peak efficiency after a little decrease. The results indicate that both the surface structure and the surface area play important roles in this reaction. The catalytic performance of materials is closely related to the specific surface area. To compare the catalytic performance of the membrane with that of powder, the kinetic rate per area has been calculated. Note that the data on powder have been taken from previous research.[28] A specific surface area of 12.08 $m^2\ g^{-1}$ of FEP powder has been measured by the Brunauer–Emmett–Teller (BET) test. We used the ratio (1.03) between the actual area derived from AFM and the shadow area to calculate the surface area of the film (0.0202 m^2). The rates for the FEP powder, FEP film, and the etched FEP film are 0.7912, 0.3227, and 0.0810 $min^{-1}\ m^{-2}$, respectively. The performance of the etched film is about 4 times higher than that of the pristine one, but still 59% lower than that of the powder. It is broadly understood that increasing the surface area can deliver a higher performance, but the relationship between the surface structure and the CEC efficiency remains unclear. We have discussed this point in the next part.

Contact-electrification measurements on surfaces

To further investigate how the surface structure of FEP influences the efficiency of contact-electrification, Kelvin probe force microscopy (KPFM) was employed to measure the electric potential of different points on the said structures as shown in Fig. 4a. KPFM is one of the most powerful and reliable tools in the study of contact electrification.[35,37,45–49] The potential distribution here can be considered as charge density distribution and contact electrification ability. Before the measurements, the samples were cleaned with ethanol and blown in front of an ion fan in order to remove the initial electrostatic charges. A KPFM probe working in the tapping mode was used to detect the surface topography and potential distribution. The surface topography as shown in Fig. 4b is consistent with the observation of SEM results shown in Fig. 2a, showing a nanoforest consisting of cone-like structures with an average diameter of ~200 nm and a height of ~120 nm, see Fig. 2b. It is worth noting that a relationship between the surface structure and the potential distribution appears, as shown in Fig. 4c. As a matter of fact, the potential distribution follows the ups and downs of the surface structure. At the summit of the peaks the highest charge densities are observed, while the lowest values are observed in the valleys between the peaks. Almost all of the peaks observed in Fig. 4c correspond to a bulged structure shown in Fig. 4b, suggesting a difference in the contact electrification between the flat surface and the modified surface. One hundred peaks were randomly selected from four etched films and calculated to investigate whether the dispersity of the height value and the potential value match or not, which can be found in Table S1.† The result in Fig. S11† shows no strong correlation between these two factors, suggesting that this difference in the charge transfer ability mainly comes from curvature.[48] The results we obtained are consistent with former research showing that convex surfaces are more conducive to electron transfer with liquid drops than concave surfaces in contact electrification at the solid–liquid interface.[50,51] This difference can be explained by the curvature-induced energy shifts of the surface states. Besides this effect, another hypothesis can be brought up. We propose that the carbon chains were broken in the peak of the structure, causing more exposure of the fluorine group, thus increasing the probability of electron cloud overlap and a better charge transfer ability, and CEC efficiency.[41]

To verify our hypothesis, Raman and ATR-FTIR (Fig. S12†) were employed to detect the surface chemical change. However, neither of these technics seemed sensitive for this purpose. Employing XPS for surface analysis led to a more conclusive result. The C 1s, F 1s, and O 1s spectra are displayed in Fig. 4d, e and f. The C 1s spectrum shows that the concentration of $C–F_3$ and $C–F_2$ increased compared to that of the pristine film, which is in good agreement with the previous hypothesis. The F 1s spectrum confirms the result obtained for C 1s. It is worth noting that the concentration of C–F is slightly higher than that of $C–F_2$. The O 1s spectra show that the amount of O–F bonds increased relatively to the amount of C–O and C═O bonds at the surface of the sample after Ar-ICP etching. To evaluate the amount of $–CF_3$ groups at the surface, we propose to use the ratio of peak area of $C–F_3$/C–C (C 1s) and C–F/$C–F_2$ (F 1s). The ratio of $C–F_3$ to C–C of the etched film (6.1076) is 6.2 times higher than that of the pristine film (0.9803) while the ratio of $C–F_2$/C–C changed only from 9.3625

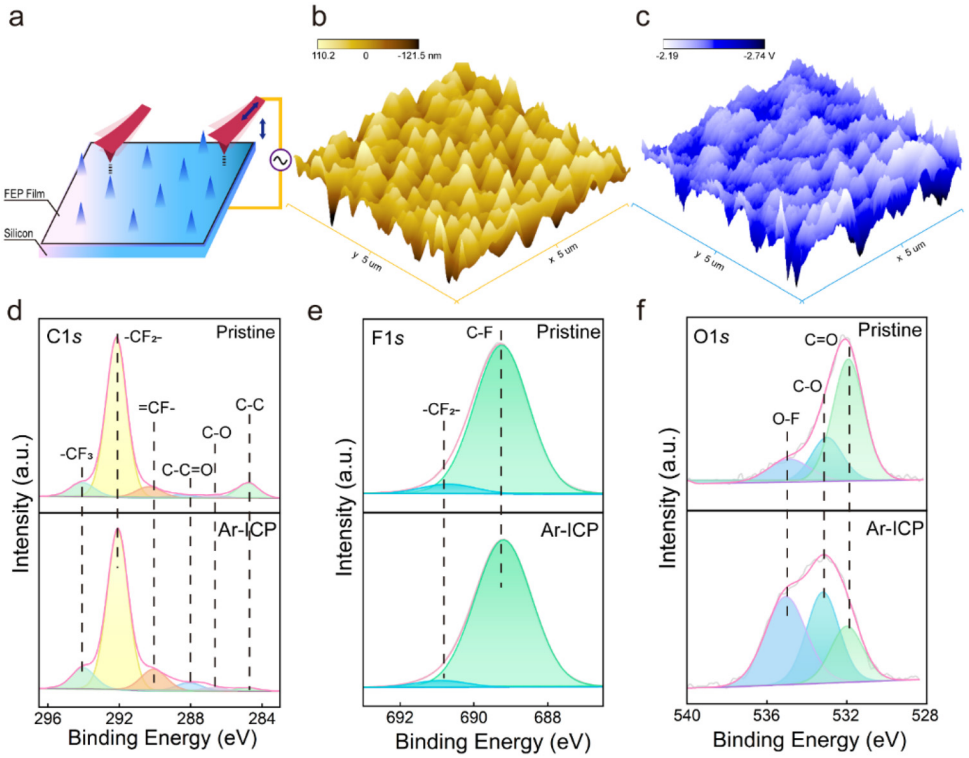

Fig. 4 Contact electrification ability of different surface structures. (a) Schematic diagram of electric potential measurement using Kelvin probe force microscopy (KPFM) for the 60 second-etched FEP film. The red patterns and blue cones represent the KPFM probe and surface structures, respectively. The dotted lines are a guide to the eye. (b) Surface structure of the etched FEP film. (c) Measured potential of the same zone of the etched FEP film. (d) C 1s, (e) F 1s, and (f) O 1s for pristine and 60 second-etched FEP films.

to 8.7679. In the F 1s result, the ratio of C–F/C–F_2 (15.859 for pristine and 24.018 for etched films) is consistent with the C 1s result. Considering that the depth of XPS analysis is only 10 nm, while our structures are ~120 nm high, we suggest that the observations on the Ar-ICP treated samples are largely influenced by the composition of the peak nanostructures.

General applicability of the method

Enhancing the performance for the degradation of MO using modified FEP films has been demonstrated in the former discussion. To investigate the generalizability of this method, several dielectric films such as polyethylene terephthalate (PET), poly tetra fluoroethylene (PTFE), and polyvinyl chloride (PVC) films have been studied. The results are shown in Fig. 5a, b, and c. The efficiency of MO degradation increased by various degrees for these different materials. None of the etched PTFE films showed good performance, and PET and PVC did not perform well, which is consistent with their charge transfer ability. Compared to PET and PVC, etched PTFE showed a better improvement. Interestingly, PTFE, a material with a high dielectric constant, did not show a big improvement compared to FEP. We suggest that the main reason for the limited enhancement of PTFE contact-electrification ability, after Ar-ICP treatment, is the result of its inability to expose a significant amount of CF_3 functional groups. In contrast to PTFE, FEP contains CF_3 groups. This

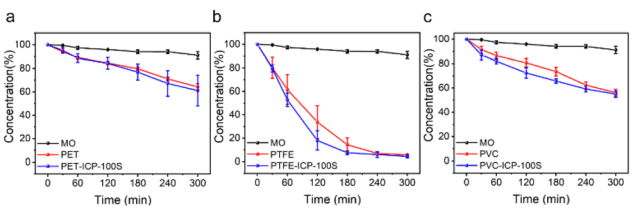

Fig. 5 CEC performance of varied material films. (a) Degradation of MO with a PET film. (b) Degradation of MO with a PTFE film. (c) Degradation of MO with a PVC film.

result matches our as-mentioned hypothesis. Meanwhile, a negligible, yet observable enhancement was observed for PET and PVC films. The same effect was detected in contact angle measurements (Fig. S13†). Although the stability of the modified films remains unsatisfactory (Fig. S14†), the results indicate that the film-based CEC can be useful for pollution treatment, and can be extended to other relevant films.

Conclusions

Degradation of methyl orange by dielectric films based on contact-electro-catalysis has been proposed and systematically investigated. Inductively coupled plasma (ICP) was introduced in the film to create surface structures, which not only

increased the surface area but also improved the contact electrification (CB) ability, thus resulting in a higher efficiency of the reaction. In our experiment, 50 ml of 5 ppm methyl orange solution was degraded to 50% after 5 hours of ultrasonication with 98 cm^2 of the pristine FEP film. This degradation efficiency could be improved by modifying the surface structure using ICP. This process performs the best after 60 seconds of etching, degrading up to 90% of the MO, in 5 hours. A ~0.7 V potential difference has been detected between the peaks and the valleys of the modified film, indicating a higher charge density on the summit of the peaks. We propose that a higher concentration of fluorine groups, observed in XPS, contributes to this difference. We anticipate that this work will pave a pathway to bring CEC to scalable applications, based on films.

Methods

Chemical reagents and materials

Methyl orange [$C_{14}H_{14}N_3NaO_3S$, Macklin, 98%], nitroblue tetrazolium chloride (NBT) [$C_{40}H_{30}N_{10}O_6Cl_2$, Macklin, 98%], terephthalic acid (THA) [$C_8H_6O_4$], sodium phosphate tribasic dodecahydrate [$Na_3PO_4{\cdot}12H_2O$, Macklin, 98%], fluorinated ethylene propylene (FEP) film [$(C_3F_6{\cdot}C_2F_4)_n$, Dupont], poly tetra fluoroethylene (PTFE) [$(C_2F_4)_n$, Guoqiang], polyvinyl chloride (PVC) [$(C_2H_3Cl)_n$, Xuling Plastics], polyethylene glycol terephthalate (PET) [$(C_{10}H_8O_4)_n$, Baosheng Engineering Plastics], high density polyethylene (HDPE) [$(C_2H_4)_n$, Guoqiang], and deionized water were used throughout the experiment.

Sample preparation

A 5 ppm aqueous methyl orange solution (MO) was prepared by adding 5 mg of $C_{14}H_{14}N_3NaO_3S$ in 1 L of ultrapure water, followed by magnetic stirring for 1 h at room temperature. The solution of THA was made by adding 332.4 mg of *p*-phthalic acid to buffer solution containing 760 mg of sodium tribasic dodecahydrate. The pH of THA was changed using HCl or NaOH. The NBT solution was prepared by diluting 8.12 mg of NBT in one liter of 0.05 M PBS buffer with a pH of 7.8. A 50 μm thick film was cut into pieces of 140 mm length and 70 mm width and then cleaned with anhydrous ethanol and DI water (18.2 MΩ cm). A thin gold layer was sputtered on both sides of the film to form a random mask using a 108Auto, Kensington, with an injection current of 20 μA for 40 seconds. The power of the plasma etching equipment (Si500, SENTECH) was 800 W, the etching gas used was argon, and the gas flow was 30 sccm. The etching time was 20, 40, 60, 80, 100, and 200 seconds, respectively. The etched film was added to a beaker containing 50 mL of the as-prepared methyl orange solution. The solution containing MO and the film was ultrasonicated (20 kHz, 900 W) using an ultrasonication bath (SBL-22DT, SCIENTZ BIOTECHNOLOGY). Aliquots (2 ml) were sampled at 0, 30, 60, 120, 180, 240, and 300 min. The water temperature was maintained at 25 °C by water circulation.

Sample characterization

The UV-Vis absorbance of the aliquots was measured using an Agilent Cary 3500 UV-Visible spectrometer in the range of 250–750 nm. The samples were placed in a Hellma Analytics QS High precision cell (Art. No. 104-10-40) with a light path of 10 mm. Scanning electron microscopy (SEM) images of the samples were obtained using a HITACHI SU8020. 5k, 10k, and 15k zoom-in resolution pictures were captured. The density of the nanoforest was calculated using Image J. All pictures were transformed into 8-byte pictures before measurement. 10k zoom-in photos were selected to calculate the density and average size. The average contact angle of the film was measured by the double-circle tangent method employing a CA100C from Shanghai INNUO. For each film, at least three random points were selected to obtain the average contact angle. The volume of the droplet was 10 μl for each measurement. X-ray photoelectron spectroscopy (XPS) was conducted on a Thermo Fisher Scientific K-Alpha, using an Alkα ray source ($h\nu$ = 1486.6 eV). The working voltage and the filament current were 15 kV and 10 mA, respectively. The pass energy was set at 30 eV. LC-MS was performed using an Orbitrap quadrupole-electrostatic field high resolution tandem mass spectrometer (Thermo &Fisher Q Exactive, USA). A −3.0 kV HESI ion source of the mass spectrometer was set. The column used was a Waters BEH C18 (2.1 × 100 mm, 1.7 μm). The temperature was set at 40 °C and the injection volume was 5 μl. The mobile phase A was composed of 0.1% formic acid aqueous solution, and the mobile phase B was an acetonitrile solution. Atomic force microscopy (AFM) was used to detect the surface roughness on an MFP-3D AFM from Oxford Instruments. Silicon-based probes with a force constant of 48 N m^{-1} and a nominal resonance frequency of 190 kHz were used. The arithmetic average of the absolute values of the profile height deviations from the mean line, also called R_a, was used to represent surface roughness. The surface area of the films was calculated using Gwyddion using three different films and the scan size was 80 × 80 μm^2. Kelvin probe force microscopy (KPFM) was employed to study the potential in the polymer surface using an MFP-3D. The tip working in the tapping mode was 25Pt400B purchased from RockyMountain Nanotechnology, USA. In KPFM scanning, the scan size was 5 × 5 μm^2 μm and the scan rate was 1 Hz. Raman spectra were recorded using a LABRAM HR EVOLUTION. A Bruker VERTEX80v with additional ATR was employed to measure the ATR-FTIR spectra. The BET test was performed with nitrogen gas in a V-Sorb2800 TP.

Author contributions

X. Z. and Y. S. contributed equally to this work. X. Z.: conceptualization, methodology, investigation, visualization. Y. S.: conceptualization, methodology, investigation, writing – original draft. A. B.: supervision, investigation. Z. L. W.: supervision, resources, funding acquisition. T. W.: supervision, writing – review and editing.

Conflicts of interest

There are no conflicts to declare.

Acknowledgements

We would like to thank Dr Huabo Zhao for his technical assistance. We appreciate Zhen Tang, Wenchao Shi, Yuan Liu, and Chengyu Li for their assistance with collecting and organizing data. The authors are grateful for the support received from the National Key R&D Project from the Ministry of Science and Technology (Grant No. 2016YFA0202704, Z. L. W.), the National Natural Science Foundation of China (Grant No. 51432005, and 5151101243, Z. L. W.), the Beijing Municipal Science and Technology Commission (Grant No. Z181100003818016, Z171100000317001, Z171100002017017, and Y3993113DF, T. W.), the Youth Innovation Promotion Association (T. W.), and the CAS-TWAS President's Fellowship (A. B.).

References

1 M. Chethana, L. G. Sorokhaibam, V. M. Bhandari, S. Raja and V. V. Ranade, *ACS Sustainable Chem. Eng.*, 2016, **4**, 2495–2507.
2 E. Routoula and S. V. Patwardhan, *Environ. Sci. Technol.*, 2020, **54**, 647–664.
3 F. I. Vacchi, A. F. Albuquerque, J. A. Vendemiatti, D. A. Morales, A. B. Ormond, H. S. Freeman, G. J. Zocolo, M. V. B. Zanoni and G. Umbuzeiro, *Sci. Total Environ.*, 2013, **442**, 302–309.
4 S. Enami, Y. Sakamoto and A. J. Colussi, *Proc. Natl. Acad. Sci. U. S. A.*, 2014, **111**, 623–628.
5 H. J. H. Fenton, *J. Chem. Soc., Trans.*, 1894, **65**, 899–910.
6 J. H. Ramirez, F. J. Maldonado-Hódar, A. F. Pérez-Cadenas, C. Moreno-Castilla, C. A. Costa and L. M. Madeira, *Appl. Catal., B*, 2007, **75**, 312–323.
7 J. Xu, X. Zheng, Z. Feng, Z. Lu, Z. Zhang, W. Huang, Y. Li, D. Vuckovic, Y. Li, S. Dai, G. Chen, K. Wang, H. Wang, J. K. Chen, W. Mitch and Y. Cui, *Nat. Sustain.*, 2021, **4**, 233–241.
8 C. Dong, Y. Yang, X. Hu, Y. Cho, G. Jang, Y. Ao, L. Wang, J. Shen, J. H. Park and K. Zhang, *Nat. Commun.*, 2022, **13**, 4982.
9 S. Rojas and P. Horcajada, *Chem. Rev.*, 2020, **120**, 8378–8415.
10 M. Patel, R. Kumar, K. Kishor, T. Mlsna, C. U. Pittman and D. Mohan, *Chem. Rev.*, 2019, **119**, 3510–3673.
11 A. S. Novikov, M. L. Kuznetsov, A. J. Pombeiro, N. A. Bokach and G. B. Shul'pin, *ACS Catal.*, 2013, **3**, 1195–1208.
12 H. Ranji-Burachaloo, P. A. Gurr, D. E. Dunstan and G. G. Qiao, *ACS Nano*, 2018, **12**, 11819–11837.
13 A. N. Pham, G. Xing, C. J. Miller and T. D. Waite, *J. Catal.*, 2013, **301**, 54–64.
14 S. Wang, *Dyes Pigm.*, 2008, **76**, 714–720.
15 B. Wang, X. Chang and H. Ma, *Ind. Eng. Chem. Res.*, 2008, **47**, 8478–8483.
16 F. Dong, Z. Pang, S. Yang, Q. Lin, S. Song, C. Li, X. Ma and S. Nie, *ACS Nano*, 2022, **16**, 3449–3475.
17 Y. Xu, M. Wang, Q. Xie, Y. Wang, X. Cui and L. Jiang, *ACS Sustainable Chem. Eng.*, 2022, **10**, 2938–2946.
18 Z.-H. Zhu, Y. Liu, C. Song, Y. Hu, G. Feng and B. Z. Tang, *ACS Nano*, 2022, **16**, 1346–1357.
19 B. Bagchi, N. A. Hoque, N. Janowicz, S. Das and M. K. Tiwari, *Nano Energy*, 2020, **78**, 105339.
20 S. Tu, Y. Guo, Y. Zhang, C. Hu, T. Zhang, T. Ma and H. Huang, *Adv. Funct. Mater.*, 2020, **30**, 2005158.
21 A. Nagar and T. Pradeep, *ACS Nano*, 2020, **14**, 6420–6435.
22 Y. Peng, S. He and F. Wu, *Sci. Total Environ.*, 2021, **775**, 145137.
23 E. Daneshvar, M. J. Zarrinmehr, E. Koutra, M. Kornaros, O. Farhadian and A. Bhatnagar, *Bioresour. Technol.*, 2019, **273**, 556–564.
24 C. P. L. Grady Jr., G. T. Daigger, N. G. Love and C. D. M. Filipe, *Biological wastewater treatment[M]*, CRC press, 2011.
25 Z. W. Seh, J. Kibsgaard, C. F. Dickens, I. Chorkendorff, J. K. Nørskov and T. F. Jaramillo, *Science*, 2017, **355**, 146.
26 J. Twilton, C. Le, P. Zhang, M. H. Shaw, R. W. Evans and D. W. C. MacMillan, *Nat. Rev. Chem.*, 2017, **1**, 0052.
27 A. M. Appel, J. E. Bercaw, A. B. Bocarsly, H. Dobbek, D. L. DuBois, M. Dupuis, J. G. Ferry, E. Fujita, R. Hille, P. J. A. Kenis, C. A. Kerfeld, R. H. Morris, C. H. F. Peden, A. R. Portis, S. W. Ragsdale, T. B. Rauchfuss, J. N. H. Reek, L. C. Seefeldt, R. K. Thauer and G. L. Waldrop, *Chem. Rev.*, 2013, **113**, 6621–6658.
28 Z. Wang, A. Berbille, Y. Feng, S. Li, L. Zhu, W. Tang and Z. L. Wang, *Nat. Commun.*, 2022, **13**, 130.
29 M. Willatzen, L. C. Lew Yan and Z. L. Wang, *Adv. Funct. Mater.*, 2020, **30**, 1910461.
30 A. W. Copeland, O. D. Black and A. B. Garrett, *Chem. Rev.*, 1942, **31**, 177–226.
31 F. Williams and A. J. Nozik, *Nature*, 1984, **312**, 21–27.
32 J. Le, Q. Fan, L. Perez-Martinez, A. Cuesta and J. Cheng, *Phys. Chem. Chem. Phys.*, 2018, **20**, 11554–11558.
33 F. Zhan, A. C. Wang, L. Xu, S. Lin, J. Shao, X. Chen and Z. L. Wang, *ACS Nano*, 2020, **14**, 17565–17573.
34 S. Li, J. Nie, Y. Shi, X. Tao, F. Wang, J. Tian, S. Lin, X. Chen and Z. L. Wang, *Adv. Mater.*, 2020, **32**, 2001307.
35 S. Lin, L. Xu, A. Chi Wang and Z. L. Wang, *Nat. Commun.*, 2020, **11**, 399.
36 C. Xu, Y. Zi, A. C. Wang, H. Zou, Y. Dai, X. He, P. Wang, Y.-C. Wang, P. Feng, D. Li and Z. L. Wang, *Adv. Mater.*, 2018, **30**, 1706790.
37 S. Lin, X. Chen and Z. L. Wang, *Chem. Rev.*, 2022, **122**, 5209–5232.
38 X. Dong, Z. Wang, A. Berbille, X. Zhao, W. Tang and Z. L. Wang, *Nano Energy*, 2022, **99**, 107346.
39 N. Zhao, B. Fu and H. B. Ma, *Appl. Phys. Lett.*, 2014, **104**, 263105.

40 Z. L. Wang and A. C. Wang, *Mater. Today*, 2019, **30**, 34–51.
41 Y. Nan, J. Shao, M. Willatzen and Z. L. Wang, *Research*, 2022, **2022**, 9861463.
42 H. Fang, W. Wu, J. Song and Z. L. Wang, *J. Phys. Chem. C*, 2009, **113**, 16571–16574.
43 X. Man, N. Bao, Y. Hao, Y. Feng and X. Ma, *Phys. Status Solidi A*, 2020, **217**, 2000223.
44 M. Sun, Q. Lu, Z. L. Wang and B. Huang, *Nat. Commun.*, 2021, **12**, 1752.
45 S. Lin, L. Xu, C. Xu, X. Chen, A. C. Wang, B. Zhang, P. Lin, Y. Yang, H. Zhao and Z. L. Wang, *Adv. Mater.*, 2019, **31**, 1808197.
46 S. Lin, L. Xu, L. Zhu, X. Chen and Z. L. Wang, *Adv. Mater.*, 2019, **31**, 1901418.
47 S. Lin, M. Zheng, J. Luo and Z. L. Wang, *ACS Nano*, 2020, **14**, 10733–10741.
48 S. Lin, M. Zheng, L. Xu, L. Zhu and Z. L. Wang, *J. Phys. D: Appl. Phys.*, 2022, **55**, 315502.
49 S. Lin, L. Zhu, Z. Tang and Z. L. Wang, *Nat. Commun.*, 2022, **13**, 5230.
50 Z. Chen, Y. Lu, R. Manica and Q. Liu, *Nano Energy*, 2021, **89**, 106456.
51 C. Xu, B. Zhang, A. C. Wang, H. Zou, G. Liu, W. Ding, C. Wu, M. Ma, P. Feng, Z. Lin and Z. L. Wang, *ACS Nano*, 2019, **13**, 2034–2041.